PAPER • OPEN ACCESS

COREDIV simulations of D and D–T high current–high power Baseline pulses in JET-ITER like wall

To cite this article: G. Telesca *et al* 2024 *Nucl. Fusion* **64** 066018

OPEN ACCESS
IOP Publishing | International Atomic Energy Agency
Nuclear Fusion
Nucl. Fusion **64** (2024) 066018 (14pp)
https://doi.org/10.1088/1741-4326/ad3bcd

COREDIV simulations of D and D–T high current–high power Baseline pulses in JET-ITER like wall

G. Telesca[1,*], A.R. Field[2], I. Ivanova-Stanik[1], S. Brezinsek[3], A. Chomiczewska[1], D. Frigione[4], L. Garzotti[2], E. Kowalska-Strzeciwilk[1], P. Lomas[2], J. Mailloux[2], G. Pucella[5], F. Rimini[2], D. Van Eester[6], R. Zagórski[7] and JET Contributors[a]

[1] Institute of Plasma Physics and Laser Microfusion, Warsaw, Poland
[2] Culham Centre for Fusion Energy, Culham Science Centre, Abingdon, Oxon, United Kingdom of Great Britain and Northern Ireland
[3] Institut fuerEnergie-und Klimaforschung-Plasmaphysik-FoschungszentrumJuelich GmbH, Juelich, Germany
[4] Università di Roma Tor Vergata, Rome, Italy
[5] Dip.to Fusione e Tecnologie per la Sicurezza Nucleare, ENEA C. R. Frascati, Frascati (Roma), Italy
[6] Laboratory for Plasma Physics LPP-ERM/KMS, Brussels, Belgium
[7] National Centre for Nuclear Research, Otwock, Poland

E-mail: giuseppe.telesca@ifpilm.pl

Received 25 October 2023, revised 20 March 2024
Accepted for publication 8 April 2024
Published 1 May 2024

Abstract

The two best performing pulses of the so called ITER-Baseline scenario ($I_p = 3.5$ MA and $P_{in} \approx 35$ MW) of JET-ITER like wall, one in deuterium (D) the other in deuterium–tritium (D–T) plasma are examined and compared in this study. Generally, the D–T Baseline pulses exhibit an electron density level higher than the D pulses and the plasma energy is higher than in the comparable D pulses by up to 20%, reaching about 12 MJ in the pulse studied here. In contrast with the D pulses, the D–T pulses are often characterised by the increase in time of the radiated power in the mantle region ($0.70 < \rho < 0.95$), which may lead to the loss of the edge localised mode activity when the threshold H–L transition power is approached and to the subsequent plasma disruption due to excessive radiation. In this study we try to identify the physical mechanisms responsible for this behaviour using the available experimental data (principally the total radiated power from the bolometry) and the results of the fluid COREDIV model (1D in the core, 2D in the scrape-off-layer (SOL)), self-consistent with respect to core-SOL and also to main plasma-impurities. In fact, the loss of power caused by impurity radiation affects the temperature profile and finally the power to the divertor plate. The electron density and temperature profiles are numerically reconstructed as well as the radiated power density profiles, indicating no major difference in impurity transport in D and D–T. Indeed, the impurity transport coefficients used in COREDIV to match the experimental radiated power profiles are similar in the two pulses. The computed tungsten sources and densities are lower in the D–T pulse and the divertor impurity retention capability is a little better in the D–T pulse,

[a] See Maggi *et al* 2024 (https://doi.org/10.1088/1741-4326/ad3e16) for JET Contributors.
[*] Author to whom any correspondence should be addressed.

indicatinga stronger collisional drag force in the SOL. The higher electron density and the broadening of its profile are the main cause of the observed increase of the radiated power in the D–T pulse.

Keywords: JET tokamak, COREDIV, modelling, impurity transport

(Some figures may appear in colour only in the online journal)

1. Introduction

In support of the development of a possible operational ITER scenario two main lines of experiments have been performed in JET-ITER-like wall (ILW) (tungsten divertor and beryllium main chamber) [1] both in D and in deuterium–tritium (D–T) plasmas. The so-called hybrid scenario [2], at a relatively low plasma current, $I_p \approx 2.3$ MA and high $\beta_N \geqslant 2.3$ with $q(0) \geqslant 1$, and the so-called ITER-Baseline scenario (henceforth Baseline) [3] at high I_p (up to and above 3.5 MA) characterised by high density, $\beta_N \approx 1.8$ and $q_{95} = 3$. Both scenarios operate in high confinement, H-mode, with auxiliary power up to about 35 MW (about 30 MW of neutral beam injection (NBI) and 4–5 MW of ion cyclotron resonance frequency (ICRF) heating and with edge localised modes (ELMs).

Given that ELMs can cause either an influx or loss of impurities from the confined plasma, it has been demonstrated [4, 5] that, in contrast with the hybrid plasmas, in the Baseline plasmas the ELMs action results in a significant impurity outflux, referred to as 'flushing', during the intra-ELM phases while during the inter-ELM phases impurities enter the main plasma.

This study is focused on data analysis and numerical simulations of recent Baseline pulses [6] and on the comparison of their characteristics in D and D–T plasmas with special emphasis on the impurity transport properties. We have analysed and numerically simulated the highest confinement Baseline D JET-ILW pulse (#96482) and the Baseline D–T pulse (#99948) with the aim of determining whether the differences in their behaviour can be explained by differences in the impurity transport and sources. Generally, the stored energy in D–T plasmas is larger (up to 12 WJ for P_{in} at about 34 MW) than that of the comparable D plasmas by about 20%, but this positive aspect of the Baseline D–T plasmas is accompanied, in the case of $I_p = 3.5$ MA, by uncontrolled increase of the radiated power leading to plasma disruption. In fact, in contrast with the hybrid plasmas which could be sustained for the full pulse duration and led to record fusion energies, the Baseline plasmas were not sustained in D–T for the required 5 s pulse duration. It is important to understand the cause of this to provide information for ITER, and, in particular, in the present study we try to understand and clarify the mechanisms responsible for the increase in radiated power during the D–T pulses. These mechanisms include the possible increase of the impurity fluxes and/or of the impurity residence time, τ_i, in D–T plasmas as compared to D plasmas as well as the effect of the increase of electron density ($P^{rad} = n_e \times n_{imp} \times L(T_e)$, where n_e is the electron density, n_{imp} is the impurity density and $L(T_e)$ is the cooling rate). This is done through analysis of the experimental data and by numerical modelling.

With respect to the implications for the data availability and for the electron density control, it is important to point out at this stage that, from the operational point of view, in Baseline scenario high confinement ($H_{98} \approx 1$) is achieved with modest gas puff level [7] and with injection of pellets of small diameter (so-called 'pacing' pellets) to assist in fuelling the plasma and in triggering ELMs, and with the divertor outer leg positioned as close as possible to the entrance of the pumping duct [3]. In fact, a major difficulty to accomplish our task relies on the absence of some essential data. Both for D and D–T Baseline scenarios the position of the outer leg close to the divertor cryopump (so-called corner configuration) results in a strike point position far from the Langmuir probes for the measurement of the electron temperature and density in the divertor. The 4 Hz sweeping of the outer strike point (in order to spread the power over a large larger area of the divertor) only marginally intercepts the line of sight (L-o-S), of the visible spectrometer devoted to the measurements of the impurity fluxes [8]. Moreover, due to the high neutron rate of the D–T plasmas, the vacuum ultra violet (VUV) spectrometer and the soft x-ray (SXR) cameras, devoted to the measurement of the tungsten density along the plasma radius, have been disconnected. Due to these difficulties, in order to compare the results of our simulations with the experimental data we have to rely essentially on the high-resolution Thomson scattering (HRTS) diagnostic, for measurement of the electron density and temperature profiles, on the charge exchange recombination spectroscopy (CXRS) for the measurement of the ion temperature profile and on the bolometric diagnostic for the measurement of the total radiated power and the radial power density profile. In fact, the bremsstrahlung Z_{eff} diagnostic provides only indications, not measurements, due to calibration issues, which are currently under investigation. However, in spite of these limitations, some physical mechanisms can be identified as responsible for the observations.

We have used the COREDIV code (see next section), which couples self-consistently simulations of the plasma core with those of the scrape-off-layer (SOL), and also the transport and radiation of impurities with the main plasma. The main inputs of the code are the plasma thermal energy, the plasma average density, the level and deposition profile of the input power and the main ion and impurity transport coefficients. In spite of some simplifications, especially in the SOL module (slab geometry and analytical model for the neutrals), the exchange of information between the core (1D) and the SOL (2D) module renders this code quite useful when, as in the case of the JET ILW and other diverted tokamak plasmas, this interaction is crucial. The numerical results are compared with the bolometric data both of the main plasma and of the SOL,

with the experimental HRTS profiles of electron temperature and density, with the ion temperature from CXRS and only qualitatively with Z_{eff} and with the BeII line intensity (see section 3).

We have considered, and analysed in detail, the two above mentioned pulses and we have modelled the D pulse at two times and the D–T pulse at three times during the pulses. For the D pulse, at a time during the stationary NBI power phase, convenient for the data analysis, and just before the end of the NBI power, and for the D–T pulse at the beginning of the stationary phase of the gas puff rate, at the time of the highest stored energy and at the beginning of the strong and fast increase in the radiated power, which leads to plasma disruption (see section 3). We have used for the simulations the stationary COREDIV code, neglecting the action of the time dependent ELM behaviour. Indeed, we have assumed that for the stationary phases of the considered pulses the impurity influx into the confined plasma and flushing action of the ELMs are balanced on a time scale of the order of the energy confinement time (see section 3.3). In spite of the fact that the ratio of impurity production to flushing is a function of the ELM frequency [9], we have compared the experimental quantities (averaged over many ELM cycles) to the results of the COREDIV simulations. Even though this procedure does not allow a time dependent analysis of the impurity production and flushing it does allow a study of the average global effective transport properties of the impurities. In fact, in COREDIV the effects of the mechanisms responsible for impurity source and transport in the SOL cause a consistent change in the confined plasma, and vice-versa, due to the core-SOL self-consistency of the code. In our numerical reconstruction, only the α-power caused by thermal plasma interaction is taken into account, neglecting the α-power originated by beam–target interaction (about 0.6 MW), which has minimal influence in the total power balance of these high heating power plasmas, see section 3.

In section 2 the main characteristics of the COREDIV code are described and section 3 is devoted to the experimental input data preparation and to the numerical reconstruction of the two considered pulses. Discussion of the results and summary of our study are presented in section 4.

2. Summary of the COREDIV code

A full description of the code is given in [10] and in section 2 of [11], while in the following only few aspects of the model, relevant for the present study, are shortly described.

- **For the plasma core**, the 1D radial transport equations are solved to calculate each ionisation state of impurity ions, bulk plasma ions and the kinetic profiles, at given experimentally volume average electron density. The local transport model proposed in [12] is used to define ion and energy fluxes.
- The anomalous diffusion coefficient of the impurities is set as $D_{\mathrm{Imp}} = D_{\mathrm{i}}$, where D_{Imp} and D_{i} are the coefficients for impurities and main ions, and for these pulses for which neoclassical (NC) convection dominates (see sections 3 and 4), inward convection [13] is adjusted as input parameter to reproduce the experimental radiation profiles. For the pulses considered in this study, with ICRF central heating, the radiation density profile can be numerically reconstructed by assigning a positive pinch velocity in the central plasma (outwards) and a negative convection at the plasma edge (inwards).
- Be, Ni and W are the impurities considered for the D plasma; to these impurities He is added for the D–T pulse. The W flux is self-consistently computed as dependent on the fluxes and energies of He, Be, Ni and on self-sputtering and the helium source is computed self-consistently according to the thermal fusion reactions, calculated to be about 60%–70% [3] of the total reactions in JET-ILW Baseline pulses. Be and Ni fluxes are code inputs (see section 3).

- **In the SOL** Braginskii-like equations [14] are the primary base of the 2D boundary layer code EPIT [15], in which the continuity and the parallel momentum equations are solved for every ion species as well as the equations for T_{e} and T_{i}, the common temperature for the main ions and the impurities.
- The parallel transport is assumed to be classical and the radial transport anomalous, with coefficients of the order of Bohm diffusion. Electrostatic, friction and thermal forces as well as atomic processes are coupled in the equations of different fluids.
- For the main ions, the electron density at the separatrix determines the recycling coefficient, which is fixed as =0.25 for Be. The sputtering yields in [16, 17] are used for hydrogenic ions and for W self-sputtering (W prompt redeposition factor of about 90%). The data in [18] are used for the W cooling rates.
- Slab geometry of the SOL module (poloidal and radial directions) implies assumption of in–out symmetry of the problem [19].
- Continuity of energy and particle fluxes as well as of particle densities and temperatures at the separatrix are imposed for the coupling between the core and SOL modules.

With respect to time-dependent self-consistent code suites like JINTRAC, see, for example, [20], the limitations of the COREDIV model refer mainly to the magnetic equilibrium, which in COREDIV is an input parameter, and to the neutral model (no Monte Carlo computation in COREDIV), apart from assuming balanced in–out impurity fluxes. On the other hand, for example, the tungsten fluxes are always computed self-consistently in COREDIV and the computing time is short (order of one day). Therefore, a full self-consistent parameter scan of some physical quantity can be performed in a time of the order of one week, thereby allowing the role of the physical mechanism to be investigated with good accuracy.

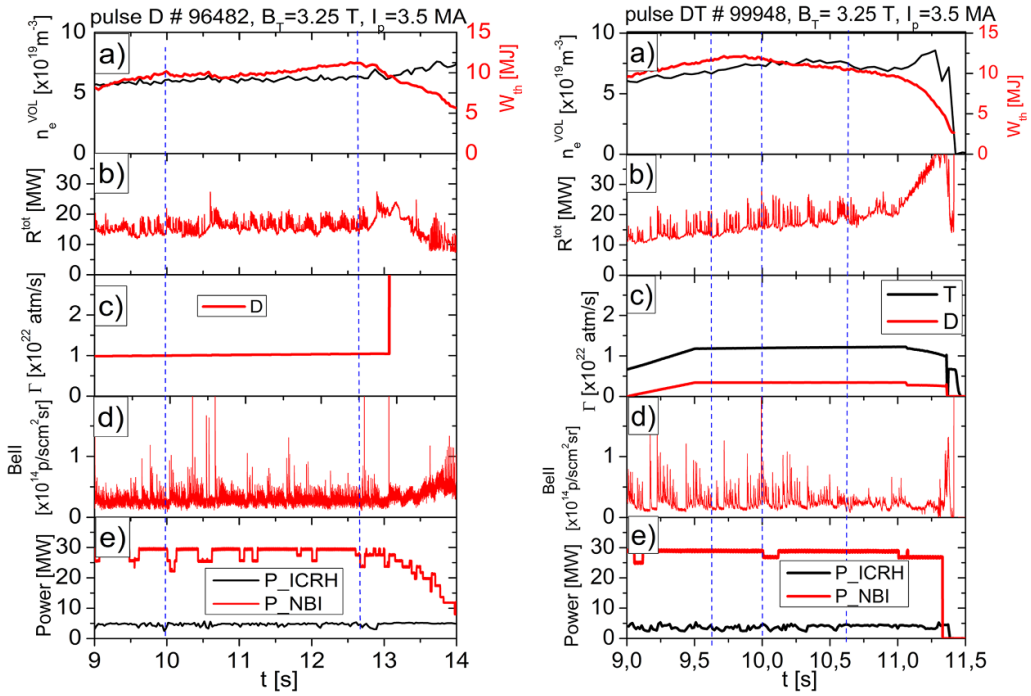

Figure 1. Some time traces of the D pulse (left) and D–T pulse (right): (*a*) volume average density and plasma energy, (*b*) total radiated power, (*c*) gas puff level, (*d*) BeII line intensity ($\lambda = 527$ nm) at the outer divertor, (*e*) power NBI and ICRF. Note the modulation of the BeII line according to the 4 Hz outer strike point sweeping.

3. Experiments and simulations

Comparison of the simulation results with the experimental observations is hampered by the absence of essential data not only due to interference from neutron emission and by the magnetic configuration chosen to reach the highest energy confinement, but also by the strong poloidal asymmetry of the W density and radiation, caused by the centrifugal forces on the W ions produced by the tangential NBI. In fact, the toroidal rotation is responsible for the localisation of the heavy impurities on the outboard mid-plane of the low field side (LFS) relatively far from the L-o-S of the spectrometer, which intercepts only marginally the W radiation (see below). The consequence of this is that also for the D pulse (for which the spectrometer was in function) the experimentally determined W concentration is not given with acceptable accuracy.

3.1. Main parameters

In the two considered pulses at $I_\mathrm{p} = 3.5$ MA and $B_\mathrm{T} = 3.25$ T at auxiliary heating power of about 34 MW, for the D pulse the electron density and the radiated power remain nearly stationary along the whole pulse duration and the plasma energy slightly increases with time, while for the D–T pulse the plasma energy starts to decrease after having reached its maximum. This is accompanied by the continuous increase of the electron density and of the radiated power, which, after having exceeded the level of the heating power, leads to the discharge disruption.

Time traces are shown in figure 1 for the auxiliary power (NBI and ICRF heating), for the total radiated power, $P^{\mathrm{rad}}{}_{\mathrm{tot}}$, for the diamagnetic energy, for the volume average electron density, for the gas puffing rate and for the BeII line intensity at the outer divertor for the D and D–T pulses. In order to assist in ELM triggering and to obtain a 50–50 D–T mixture for the D–T pulse, D-pacing pellets are injected at a throughput of 1×10^{22} electrons s^{-1} (henceforth e s^{-1}) in both pulses with a frequency of 25 Hz and 35 Hz for the D and D–T pulse, respectively. While the NBI power is the same in the two pulses, for the D–T pulse the ICRF power is about 4 MW, i.e. 1 MW less than for the D pulse, due to the unavailability of one of the radiofrequency antennas during D–T operation. This difference in auxiliary power level is *quantitatively* overcompensated by the total thermonuclear α-power (thermal + beam–target), which is about 1.6 MW. Note that the contribution of the α-particles to the total W sputtering is negligible (order of 10^3 particles s^{-1}, henceforth p s^{-1}) due to the low α-particle flux (order of 10^8 p s^{-1}) and to the very low sputtering yield in the range of the edge temperature of this pulse. The dashed vertical lines indicate the times at which the numerical simulations are performed for the two pulses. While in the D pulse the electron density is nearly constant during the pulse (apart from a tiny step at about 10.5 s, clearly seen in $P^{\mathrm{rad}}{}_{\mathrm{tot}}$) in the D–T pulse the electron density increases continuously during the pulse until ≈10.3 s, as does the radiated power. The second time selected for the simulations of the D pulse (12.6 s) is correlated with the end of the NBI power and with the increase of the plasma energy to

10.8 MJ, as compared to 9.8 MJ at 10.0 s. The three times selected for the D–T pulse correspond to the times when the gas puff rate reaches its stationary value (9.64 s), to the time the plasma energy starts to decrease (≈10.0 s) and to the beginning of the strong increase in $P^{\mathrm{rad}}{}_{\mathrm{tot}}$ (10.6 s). Note that for the D–T pulse the time 10.6 s is correlated with the start of the decrease of the ELMs level (H–L threshold ≈ 12–13 MW). At this time the plasma energy decreases to 10.7 MJ from the level 11.9 MJ at 10.0 s. Even though the total gas puff level of the D–T pulse at its stationary value is about 60% higher than that of the D pulse, its value is significantly lower than that used in the less performant (due to gas puffing) JET pulses in D where a larger scan of gas puffing is available. For both pulses $f_{\mathrm{RAD}} = P^{\mathrm{rad}}{}_{\mathrm{tot}}/P_{\mathrm{in}}$ reaches ≈ 0.45–0.50, which apparently is an upper limit for these Baseline pulses without impurity seeding.

Not only the time evolution of the average electron density is different in the two pulses, but also the density profiles show significant differences. For the D pulse the density profile is peaked all along the pulse, while for the D–T pulse it is hollow or flat, with higher density pedestals.

In figure 2 the experimental electron density (n_{e}) and temperature (T_{e}) profiles from HRTS and the CXRS ion temperature (T_{i}) profiles are shown, as an example, at 10.0 s and at 12.6 s for the D pulse and at 10.0 s and 10.6 s for the D–T pulse and are compared with the simulated profiles from COREDIV. Within the uncertainties of the measurements and of the simulations, the electron density and the ion temperature increase at the later time of the D pulse while T_{e} and T_{i} clearly decrease at the later time of the D–T pulse. The density pedestal is higher in the D–T pulse, as expected [21], and the temperature at the pedestal seems to be a little lower. The experimental core density profile is rather flat (even hollow) in the D–T pulse while it is peaked in the D pulse. The simulated profiles are obtained using as input data to the code the volume average density, $<n_{\mathrm{e}}>$, the density at the separatrix, $n_{\mathrm{e\_sep}}$, the thermal energy and the profiles of energy and main particle diffusion coefficients (please, see section 2). Note, that no convective pinch is assumed for the main ions. In table 1, some experimental and simulated values of the main parameters of the D and D–T pulses, respectively, are shown. (The simulated values are computed by imposing convective velocities for the impurities, see below). The Ni fluxes input to COREDIV (2.0×10^{19} p s^{-1} and 1.25×10^{19} p s^{-1}, for the D and D–T pulse, respectively) have been adjusted in order to reproduce the experimentally determined radiated power of Ni using the VUV spectrometer (with horizontal L-o-S), which is 1.2–1.7 MW for the D pulse and 0.9–1.3 MW for the D–T pulse [8]. For the BeII line ($\lambda = 527$ nm) intensity, measured at the outer divertor target, apart from the above mentioned partial overlapping of the L-o-S with the outer strike point, it was not possible to subtract the continuum radiation from the BeII line intensity, due to significant reflections in the divertor. Considering that the experimental background level of the BeII line is a little higher for the D pulse than for the D–T pulse (figure 1), as it is the computed ionisations per photon ($S/XB = 50$ and 42, respectively) from ADAS data [22], the COREDIV input Be flux has been set as 1.6 and 1.1×10^{21} p s^{-1} for the D and D–T pulse, respectively. Once the COREDIV input Ni fluxes are determined to match with the experimental Ni radiation level, in the absence of experimental data of the absolute Be fluxes, the Be fluxes in the code have to be chosen in such a way to reproduce the measured bolometric data. Indeed, changing the input Be fluxes the total simulated radiated power and its radial density profile also change, due to modifications of the W sputtering caused by impinging Be.

In COREDIV the time-averaged residence time of tungsten is calculated as $\tau_{\mathrm{W}} = N_{\mathrm{tot\_W}}/\Gamma_{\mathrm{Wsep}}$ where $N_{\mathrm{tot\_W}}$ is the total W content in the pulse and Γ_{Wsep} is the W flux at the separatrix, which is generally significantly lower than that at the target plate as a consequence of the impurity screening in the SOL (see below). τ_{W} is similar in the two pulses and while in the D pulse τ_{W} does not evolve in time, in the D–T pulse it is 20% higher at 10.6 s with respect to the earlier two times. The computed W flux at the target is lower for the D–T pulse by ≈20% (apart from the lower Be content), mainly as a consequence of the lower electron temperature at the divertor target, $T_{\mathrm{e\_plate}}$, in a range of temperatures for which the W sputtering yields by Be, Ni and self-sputtering increase with temperature. The computed tungsten concentration, c_{W}, is also lower in the D–T pulse than in the D pulse due both to the lower W influx and to the higher electron density. The calculated total W content, $N_{\mathrm{tot\_W}}$, is 7.84 and 8.4 $\times 10^{17}$ atoms for the D pulse and 6.31, 6.54 and 6.9 $\times 10^{17}$ atoms for the D–T pulse at the times considered. Note that the ratio of the total W content of the two pulses can also been estimated, semi-quantitatively, independently of the COREDIV results. Indeed, using the experimental data of $P^{\mathrm{rad}}{}_{\mathrm{tot}}$ and $<n_{\mathrm{e}}>$ in table 1 and assuming that the total radiation is produced by W only (in fact, the calculated fraction of W radiation to the total, $P^{\mathrm{rad}}{}_{\mathrm{W}}/P^{\mathrm{rad}}{}_{\mathrm{tot}}$, is about 0.7) and that the cooling rates are the same for the two pulses, as in [4], recalling that $P^{\mathrm{rad}}/L(T_{\mathrm{e}}) = n_{\mathrm{e}} \times n_{\mathrm{W}}$ (where $L(T_{\mathrm{e}})$ is the cooling rate), one can easily estimate the ratio of $N_{\mathrm{tot\_W}}$ for the two pulses. This gives fractions of the W content in the D–T pulse to that in the D pulse at 12.6 s, i.e. $N_{\mathrm{tot\_W}}/N_{\mathrm{tot\_W(D\ at\ 12.6.s)}}$, = 0.83, 0.82 and 0.96 at 9.64 s, 10.0 s and 10.6 s respectively, in qualitative agreement with the COREDIV results. This estimation confirms that the W content in the D–T pulse at 9.64 s and at 10.0 s is lower than that in the D pulse at 12.6 s and only at the later time approaches that in the D pulse. The choice of comparing the three values of the D–T pulse with that of the D pulse at $t = 12.6$ s is due to the level of $P^{\mathrm{rad}}{}_{\mathrm{tot}}$, which is not very different at the selected times of the two pulses. Note that, within the uncertainties of the COREDIV modelling, significant differences are not seen in the W source and transport in the D–T pulse from 9.64 s until 10.0 s, i.e. over a time interval of about two confinement times τ_{W}.

The lower computed c_{Be} in the DT pulse depends on the experimentally higher electron density as well as on the lower assumed Be influx input to the simulations.

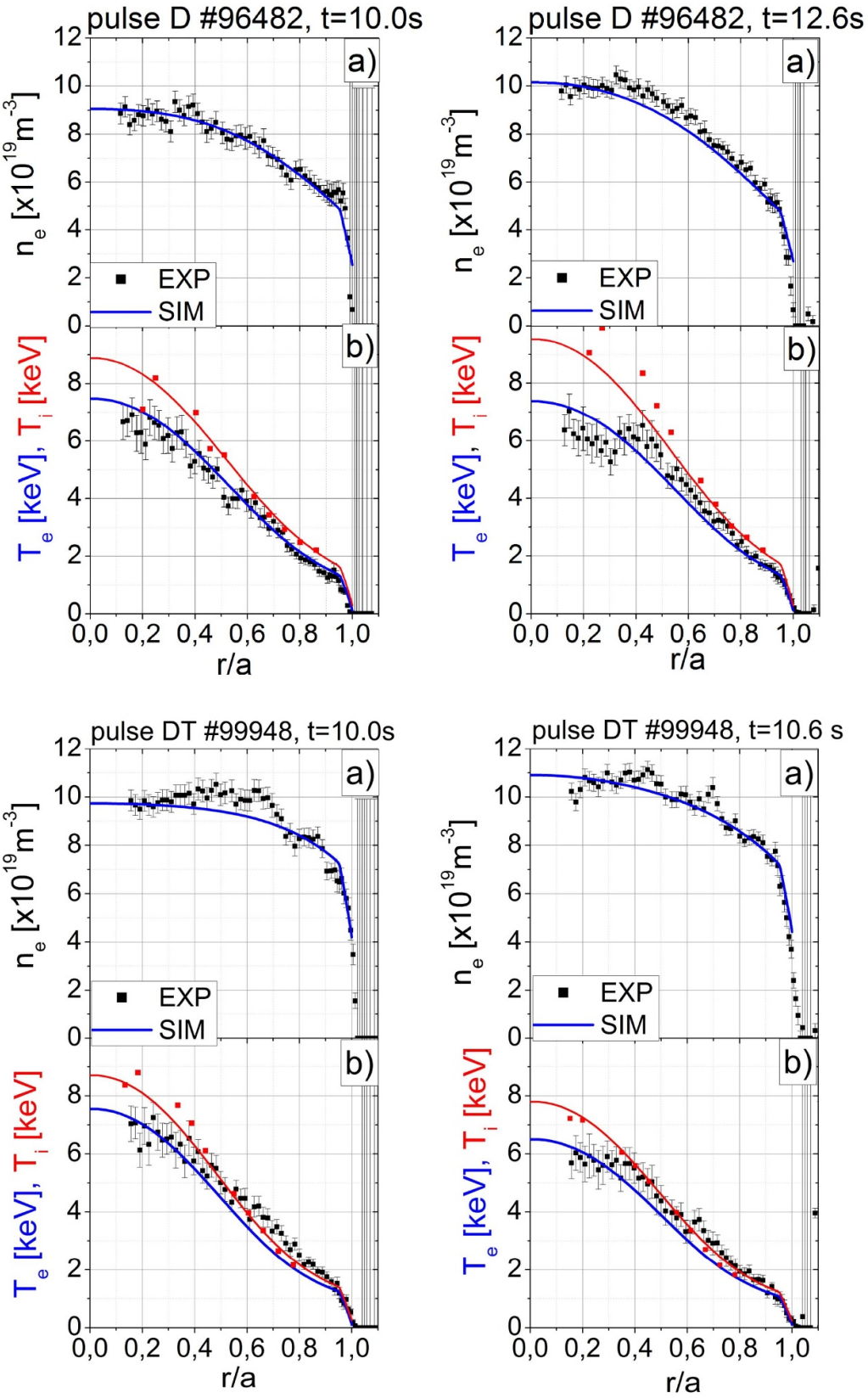

Figure 2. Examples of the experimental: (*a*) electron density profile, (*b*) electron and ion temperature profiles for the D pulse (left) and for the D–T pulse (right) at two times for each pulse and the corresponding COREDIV computed profiles.

Table 1. Experimental and numerical (*) values of relevant parameters of the two pulses: volume averaged electron density, Z_{eff}, plasma energy, total radiated power, W residence time, electron temperature at the plate, Be concentration, W flux and W concentration.

Pulse#	$<n_e>$ ($\times 10^{19}$ m^{-3})	Z_{eff}*	W_{th} (MW)	P^{rad}_{tot} (MW)	τ_W* (s)	T_{e_pl}* (eV)	C_{Be}* ($\times 10^{-2}$)	Φ_W* ($\times 10^{19}$ s^{-1})	C_W* ($\times 10^{-4}$)
				$t = 10$ s					
96 482 D	6.0	1.5	9.8	14.2	0.165	23.7	1.52	5.8	1.17
				$t = 12.6$ s					
	6.3	1.47	10.8	15.6	0.166	21.8	1.23	6.19	1.2
				$t = 9.64$ s					
	6.95	1.31	11.6	14.3	0.168	18.5	0.9	4.9	0.79
99 948 D–T				**$t = 10.0$ s**					
	7.4	1.30	11.9	15.0	0.172	18.2	0.92	5.2	0.76
				$t = 10.6$ s					
	7.5	1.31	10.7	18.0	0.198	16.0	1.17	4.7	0.80

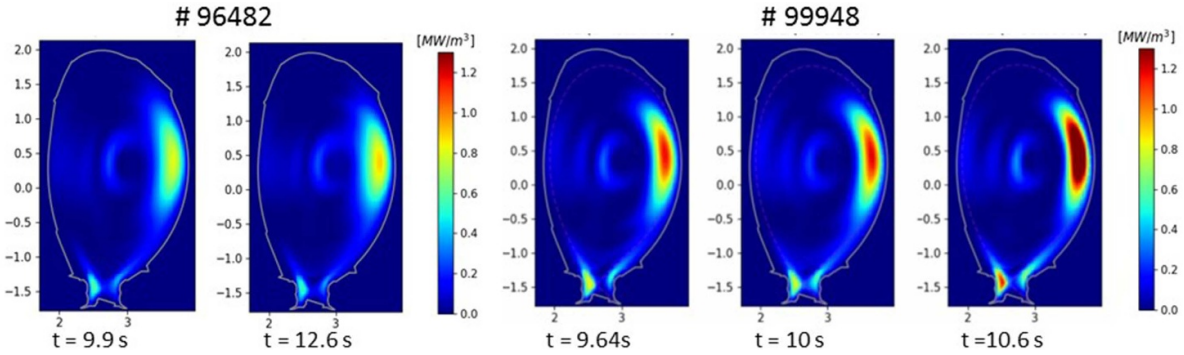

Figure 3. Tomographic reconstruction of the radiated power density at times $t = 10.0$ s and $t = 12.6$ s for the D pulse (left) and at $t = 9.64$ s, $t = 10.0$ s and $t = 10.6$ s for the D–T pulse (right).

3.2. Experimental radiation patterns and their numerical reconstructions

Tomographic 2D reconstructions of the radiation density of the D pulse are shown in figure 3 at 10.0 s and 12.6 s and for the D–T pulse at 9.64 s, 10.0 s and 10.6 s. Since the COREDIV calculations do not take into account poloidal asymmetry in the plasma core (which are experimentally caused by the toroidal rotation), the simulation results are compared with the profiles of the flux-surface averaged emissivity, as shown in figure 5. It can be observed that the intensity of the radiation in the inner divertor (independent of the W density and dependent on the electron density) increases with the intensity of the LFS radiation in the main plasma (dependent on the W density and on the electron density), suggesting that the higher radiation in the D–T pulse depends more on the higher electron density than on the W density. We note that the 2–3 semi-circles of strong radiation in the HFS starting from the plasma centre are an unavoidable artefact of the experimental reconstruction, originated from reflections in the plasma core of the divertor radiation.

MHD analysis confirms that these HFS semi-circles are independent of mode activities (hence are artefacts) and also illustrates some basic differences between the D and the D–T pulses.

It can be seen in figure 4 that the pulse #96 482 is characterised by long-period sawteeth ($T = 0.9$–1.0 s) sometimes triggering tearing modes (TMs), with toroidal mode number $n = 4, 5$, not affecting the plasma confinement. For the pulse #99 948 an ELM-triggered $n = 4$ mode is observed from 9.72 s, not reaching such amplitude as to influence the global confinement properties. A sawtooth-triggered $n = 3$ mode is observed from 10.12 s, with a relatively low amplitude (0.2 G) up to 10.27 s, a first increase between 10.27 and 10.37 s, a second stationary phase up to 10.60 s (0.6 G) and a following strong increase, with the maximum amplitude reached at 10.75 s (1.8 G). Therefore, in contrast to the D pulse, in the D–T pulse significant mode activity starts at ≈10 s, possibly triggered by a change in the gradients of the current density profile, as in [23].

From this brief investigation of the MHD data we note that the TM mode evolution in the two pulses is clearly different, and does not depend on the different level of the total radiated power P^{rad}_{tot}. In fact the different behaviour in the D–T pulse starts at times at which the level of P^{rad}_{tot} is comparable to that of the D pulse at 12.6 s.

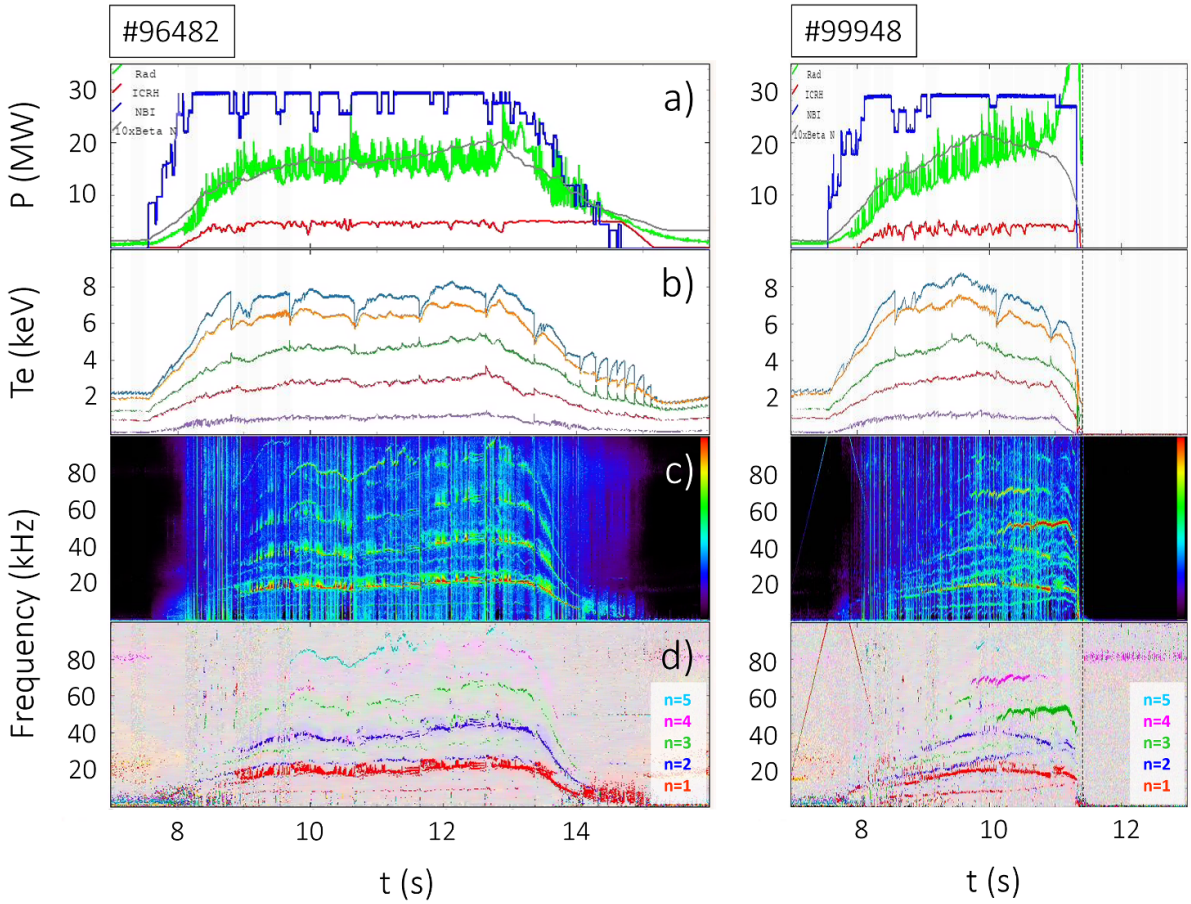

Figure 4. MHD analysis of the D pulse (left) and the D–T pulse (right): (*a*) NBI (blue) and ICRH (red) powers, total radiated power (green) and normalised beta (grey), (*b*) electron temperature at different radii, (*c*) spectrogram of mode amplitudes and (*d*) spectrogram of toroidal mode numbers from Mirnov coils.

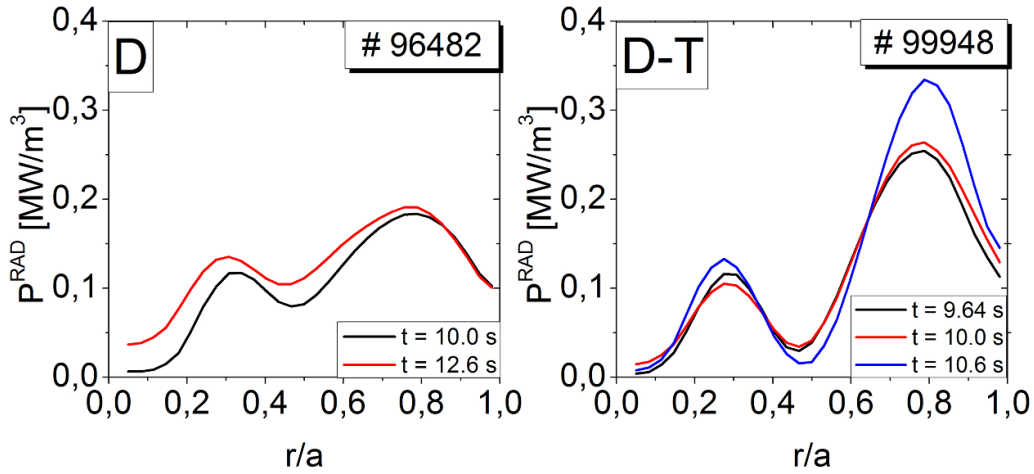

Figure 5. Experimental reconstruction of 1D radial profiles of the radiated power density, as derived from the 2D plots of figure 4. Left for the D pulse at $t = 10.0$ s and $t = 12.6$ s and right for the D–T pulse at $t = 9.64$ s, $t = 10.0$ s and $t = 10.6$ s.

In figure 5 flux-surface averaged profiles of the total radiated emissivity from the tomographic reconstruction of the bolometry data are shown, where the normalised flux coordinate, ϕ_N, has been substituted by the normalised minor radius for the comparison with the 1D numerical COREDIV results of the plasma core. It is seen that at large radii the radiation density is significantly higher in the D–T pulse while the level of the radiation arising from the artefacts in the plasma core is similar in the two pulses. The radiation densities at the two times of the D pulse are similar

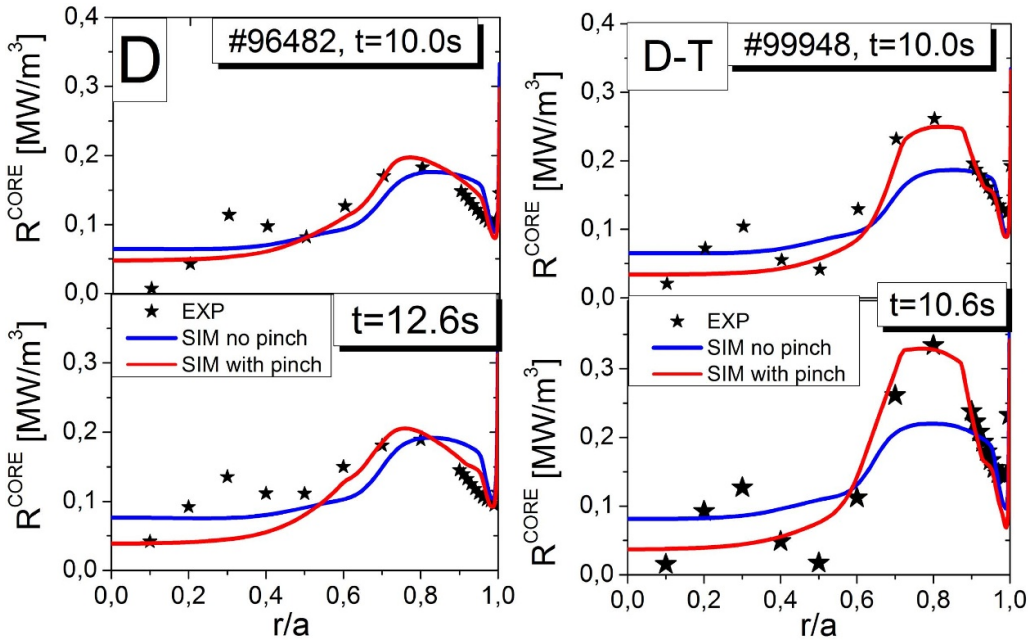

Figure 6. Examples of COREDIV radiated power density profiles for the D pulse (left) and D–T pulse (right). The blue line refers to the hypothesis of impurity diffusive transport only and the red one to diffusive + convective transport. The stars are some experimental points from the plots of figure 5.

to each other as are those at 9.64 s and 10.0 s of the D–T pulse and only at 10.6 s the radiation is significantly higher. The plots of figure 5 are used to compare the experimental data with the results of the numerical simulations, as done in figure 6. In this figure, together with few points of the experimental values of figure 5, some numerically reconstructed radiation density profiles are shown for the times of the D and D–T pulses considered, as examples. The blue curves are obtained by assuming only diffusive impurity transport while the red curves are calculated assuming an '*ad hoc*' radial convective velocity as a code input, in order to better match the experimental profiles. In the numerical reconstruction of the experimental radiation, only a relatively small inward impurity pinch is needed in the zone between the separatrix and the top of the pedestal (on the transport barrier) and an outward pinch is needed in the central plasma region, see section 4.

Given the strong density gradients between the separatrix and the top of the pedestal in these Baseline pulses, from NC theory of impurity transport one would expect a strong W inward convective velocity [4, 5]. The related strong radiation at the very edge of the plasma is, however, not seen in the tomographic reconstruction, instead a quite broad region of strong radiation localised at the mantle region ($0.7 < \rho_N < 0.95$), just inside the pedestal top. That this region of strong radiation is quite broad could be due to two reasons. Firstly, the bolometry has a finite spatial resolution, so the region of strong radiation could be more localised than it is measured. Or secondly, the radial impurity distribution results from a balance of turbulent diffusion and NC convection, with the former acting to smear out the localisation due to inward and outward convection, so the radial W density distribution will be less sharply localised than that calculated assuming convection alone.

3.3. Time-dependent data analysis

The analysis of time-dependent data helps to clarify the physical mechanisms involved in the behaviour of the considered pulses. As explained in detail in section 2.5 of [4], an estimate of the efficacy of each ELM at flushing the W impurities from the confined plasma (and also their influx during the inter-ELM periods) can be obtained from an analysis of fast bolometric total radiation measurements, using a method first applied to JET-ILW plasmas described in [24]. For this analysis we use a fast radiated power signal P^{Hor}_{Rad} calculated from a weighted sum of intensities from a bolometer camera viewing the main chamber horizontally from the LFS. With the assumption that the total radiated power is dominated by the mantle region ($0.7 < \rho_N < 0.95$) by W and considering that the cooling rate of W is rather constant ($L_W(T_e) \approx 3.5 \times 10^{-31}$ Wm^3) over the mantle region—as from the analysis of T_e profiles of typical high-current Baseline JET-ILW pulses—the W density in the mantle, n_{Wm}, can be derived from (P^{Hor}_{Rad} /Vol)/($L_W \times n_{em}$)= n_{Wm}, where n_{em} is the electron density in the mantle and Vol is the volume of the mantle region.

In panel (*a*) of figure 7 the time-dependent traces of the radiated power and of the W concentration *in the mantle region* of the two pulses are shown. Considering that the W radiation actually accounts for about 70% of the total radiated power, it follows that the W concentration in the mantle, c_{Wm}, in figure 7

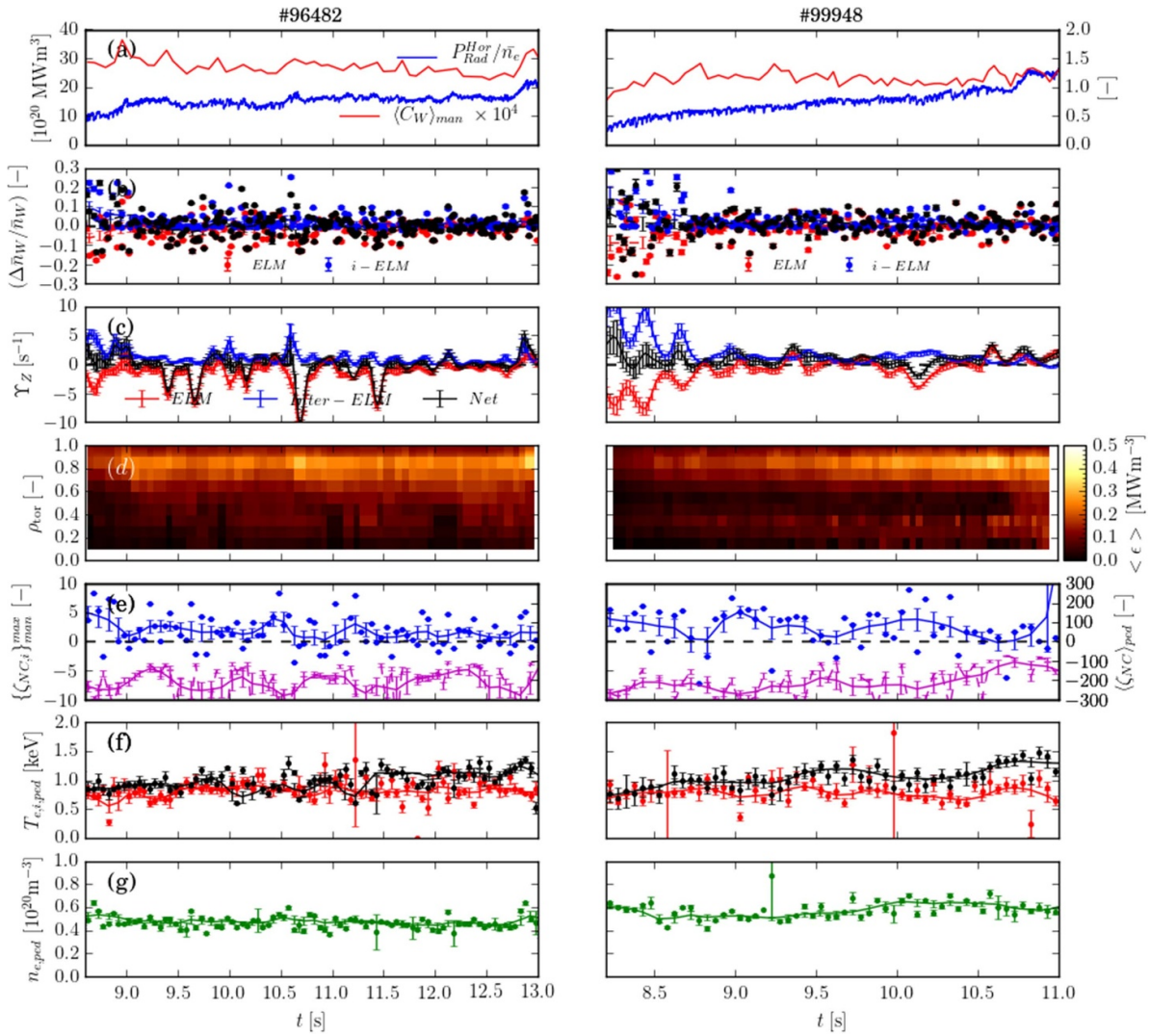

Figure 7. A comparison for the two high-power, 3.5 MA/3.3 T Baseline-scenario JET-ILW pulses (left D pulse, right D–T pulse), showing the evolution of: (*a*) the signal $P^{\mathrm{Hor}}{}_{\mathrm{Rad}}/{}^{-}ne$ (blue) and the estimated average W concentration over the mantle region $\langle C_{\mathrm{W}}\rangle_{\mathrm{man}}$ (red); (*b*) the fraction of W flushed per ELM $(\Delta^{-}n_{\mathrm{W}}/{}^{-}n_{\mathrm{W}})_{\mathrm{ELM}}$, red, the inter-ELM W influx $(\Delta^{-}n_{\mathrm{W}}/{}^{-}n_{\mathrm{W}})_{\mathrm{i-ELM}}$, blue and the net fractional change in W content per ELM cycle, black; (*c*) the respective rates of change of the W content $\gamma_{\mathrm{W}} = \mathrm{d}(\Delta^{-}n_{\mathrm{W}}/{}^{-}n_{\mathrm{W}})/\mathrm{dt}$ due to the ELM flushing ($\gamma_{\mathrm{ELM\ W}}$—red), the inter-ELM influx ($\gamma_{\mathrm{i-ELM\ W}}$—blue) and the resulting net rate of change ($\gamma_{\mathrm{net\ W}}$—black), (*d*) the flux-surface-averaged total emissivity $\langle\epsilon_{\mathrm{tot}}\rangle$ from bolometry; (*e*) the neo-classical convection parameter $\langle\zeta_{\mathrm{NC}}\rangle_{\mathrm{man}}$ averaged over the mantle region, blue, and in the pedestal, purple; (*f*) the electron $T_{\mathrm{e,ped}}$ (red) and ion $T_{\mathrm{i,ped}}$ (black) pedestal temperatures and (*g*) the pedestal density, $n_{\mathrm{e,ped}}$.

is a factor ≈1.4 higher than that computed by COREDIV. For both pulses, c_{Wm} slightly decreases vs time, for the D pulse from about $t = 10.5$ s up to the end and for the D–T pulse from about $t = 9.5$ s to about $t = 10.3$ s. Considering that for the D–T pulse the average electron density (figure 1), as well as $n_{\mathrm{e\text{-}ped}}$ in panel (*g*), increases up to 10.3 s and then slightly decreases, this shows that n_{W} for the D–T pulse remains nearly constant at least up to 10.3 s. This is in line with the plots of panel (*b*) and (*c*), which show that, on the average, the in–out W fluxes are balanced. Panel (*b*) shows the fraction of W flushed per ELM $(\Delta n_{\mathrm{W}}/n_{\mathrm{W}})_{\mathrm{ELM}}$, (red dots), the inter-ELM W influx $(\Delta n_{\mathrm{W}}/n_{\mathrm{W}})_{\mathrm{i-ELM}}$ (blue dots) and the net fractional change in W content *per ELM cycle* (black dots). Panel (*c*) shows the respective rates of change of the W content $\gamma_{\mathrm{W}} = \mathrm{d}(\Delta^{-}n_{\mathrm{W}}/{}^{-}n_{\mathrm{W}})/\mathrm{dt}$ due to the ELM flushing ($\gamma\mathrm{ELM}_{\mathrm{W\_red}}$), the inter-ELM influx ($\gamma\mathrm{i{-}ELM}_{\mathrm{W\_blue}}$) and the resulting net rate of change ($\gamma\mathrm{net}_{\mathrm{W\_black}}$). From these two plots it is clear that the average in–out W flux is balanced (i.e. ≈ 0) in the time-range of our interest. With respect to the D–T pulse, starting from about 10.3 s, n_{W}, which results from the outward pinch in the plasma core and the inward pinch in the pedestal, increases with time, due to the reduced flushing action by the ELMs and to possible change in impurity residence time. Therefore the in–out W fluxes are no longer balanced and n_{W} increases. Note, that the increase of n_{W} after 10.3 s can simply be inferred from the *increase* of the radiated power (see figures 1 and 4) and from the simultaneous slight *decrease* of both the average electron density (figure 1) and that at the pedestal (panel *g*) of figure 7). To this point, it is useful to recall the increase in the $n = 3$ mode amplitude observed to start

at about 10.3 s (see section 3.2). The flux-surface-averaged total emissivity $\langle\epsilon_{tot}\rangle$ from bolometry shown in panel (*d*) can be compared with the poloidally resolved radiation densities of figure 3. The data in panel (*e*) show the time traces of the function ζ_{NC}, which is a proxy for the NC impurity convective velocity. According to this function, defined in equation (1) of [5] as $\zeta_{NC} = (R/2L_{Ti}) - R/L_{ni}$ where L_{Ti} and L_{ni} are the scale length of the ion temperature and ion density, when the condition $R/2L_{Ti} > R/L_{ni}$ is satisfied the NC convection is outward and vice versa. Note that, for practical reasons, the scale length of the density is computed using the electron density and not the ion density profile. The slightly higher outward NC pinch in the mantle—blue line—for the D–T pulse up to 10.3 s arises from the flatter n_e profile and the higher inward NC pinch in the pedestal region—purple line—from the steeper electron density gradient across the pedestal. Please, note the increase of $T_{i,ped}$—black line, panel (*f*)—for the D pulse at about 11.3 s, which leads, together with the increase of T_i in the plasma core to the increase in the thermal energy, as seen in figures 1 and 2. One of the consequences of the above reported time-dependent data is that while the assumption made in the COREDIV model of balanced in–out W flux (i.e. average zero net W influx) is fully valid for the two simulations of the D pulses and for the simulations of the D–T pulse at 9.64 s and at 10.0 s, but might be less valid at $t = 10.6$ s.

3.4. SOL properties

Due to the lack of T_e and n_e measurements from Langmuir probes in the SOL, we have to rely only on the numerical results and on the bolometric data, which show that the radiated power in the SOL, P_{DIV}, increases with the volume average density $<n_e>$ of the pulses: $P_{DIV} = 2.1$ MW and 2.4 MW for the D pulse and 2.5 MW and 2.7 MW for the DT pulse at times 9.64 s and 10.0 s. In COREDIV the densities at the separatrix—given as input parameters—are chosen so that the experimental P_{DIV} are numerically reconstructed. Given also that for both pulses the perpendicular particle diffusion coefficient in the SOL, D_{SOL}, is set to be $D_{SOL} = 0.15$ m^2 s^{-1}, the computed T_e at the target plate (T_{e_pl}) are reported in table 1.

The ratio Γ_W/Φ_W, where Γ_W is the W flux across the separatrix and Φ_W is the W flux at the target plate, can be computed in COREDIV resulting in $\Gamma_W/\Phi_W = 8.2$ and 7.4×10^{-2} for the D and D–T pulse, respectively, implying that the divertor impurity retention is better for the D–T pulse. In general, impurity retention capability in the divertor is related to the ratio of the collisional drag force (towards the target plate) to the ion gradient thermal force (towards the separatrix) [25], and, from the practical point of view, good retention capability is obtained if $M_p > \lambda_{ii}/\lambda_T$ where M_p is the Mach number, λ_{ii} is the main ion mean free path and λ_T is the ion temperature gradient length, as estimated in [26]. Considering that for these plasmas the Mach number is $M_p \approx 0.2$ and λ_{ii}/λ_T is smaller by an order of magnitude, the impurity retention capability is inversely proportional to λ_{ii}/λ_T. This is consistent with the increased SOL impurity retention computed by COREDIV for the D–T pulse for which $\lambda_{ii}/\lambda_T \approx 1.5 \times 10^{-2}$ as compared to $\lambda_{ii}/\lambda_T \approx 2.4 \times 10^{-2}$ for the D pulse.

4. Discussion and summary

From collisional and NC theory of impurity transport, if the impurity ions are in the Pfirsch–Schlueter regime, and the hydrogenic ions in the plateau or banana regime, the stationary impurity density profile is dependent on that of the main ions in such a way that [27] to a peaked main ion density profile is associated impurity accumulation while to a flat density profile and peaked temperature profile is associated an impurity screening effect. The W density profile, $n_W(r)$, as derived by COREDIV for these pulses (see figure 8) shows the maximum of n_W in the region $r/a \approx 0.6$–0.8 resulting from the inward convective velocity in the edge region and from the outward convective velocity in the core region, which are both needed as a code input to reconstruct the experimental radiation profiles. The screening effect in the central plasma is caused by the ICRF central heating, due both to the increase of the central plasma temperature and to the action of sawteeth, which expel the impurities towards the plasma edge. On the other hand, at the very edge of the plasma between the pedestal top and the separatrix the NC theory predicts for these conditions a very strong inward impurity convection, due to the very strong negative density gradients in that region, as seen in the fast time-traces of figure 7. An order of magnitude calculation for the time-averaged NC inward pinch velocity in this region, based on the expression $V_I = 2q^2DZ\zeta_{NC}/R$ (see [5]), gives $V_W \approx -50$ m s^{-1} for W with $Z = 10$. Such a strong inward pinch is not needed in the COREDIV inputs to fit the experimental radiation density profiles of the two pulses (see figure 8). Independently of the possible effects on NC impurity convection flux caused by in–out impurity density asymmetry [28], this difference arises from the combined effect of the strong NC inward convection across the pedestal during the inter-ELM periods and the intra-ELM flushing, which are almost in balance as long as the ELMs do not disappear (see figure 1).

With respect to the different radial position of the maximum of n_W in D and D–T pulses, as shown in figure 8, that is a consequence of the changes in NC convection due to different T_i and n_i profile shapes between the D and D–T pulses.

With respect to the lower calculated W flux in the D–T pulse, it might be observed that also from the experimental point of view we might expect, heuristically, a lower time-averaged W influx in the D–T pulse. In fact, recalling that for impinging energy below ≈250 eV (≈50 eV electron temperature at the target plate) the W yield of both D and T is negligible, for the inter-ELM phases of the pulses the W influx should be lower for the D–T pulse in consideration of the computed lower temperature at the target (see table 1) in a temperature range for which the W sputtering yield by Be, Ni and self-sputtering is a strong increasing function of the temperature. For the intra-ELM phases, the W yield of a 50%–50% D–T plasma is about 50% higher than that of a D plasma for impinging energy >1 KeV. However, since the net W sputtering yield is an increasing function of the Be content, figure 2 in [29], the background intensity of time traces of the Be II line in figure 1 (ELMs modulated by the strike point sweeping at 4 Hz), as well as the lower Be flux needed as COREDIV input

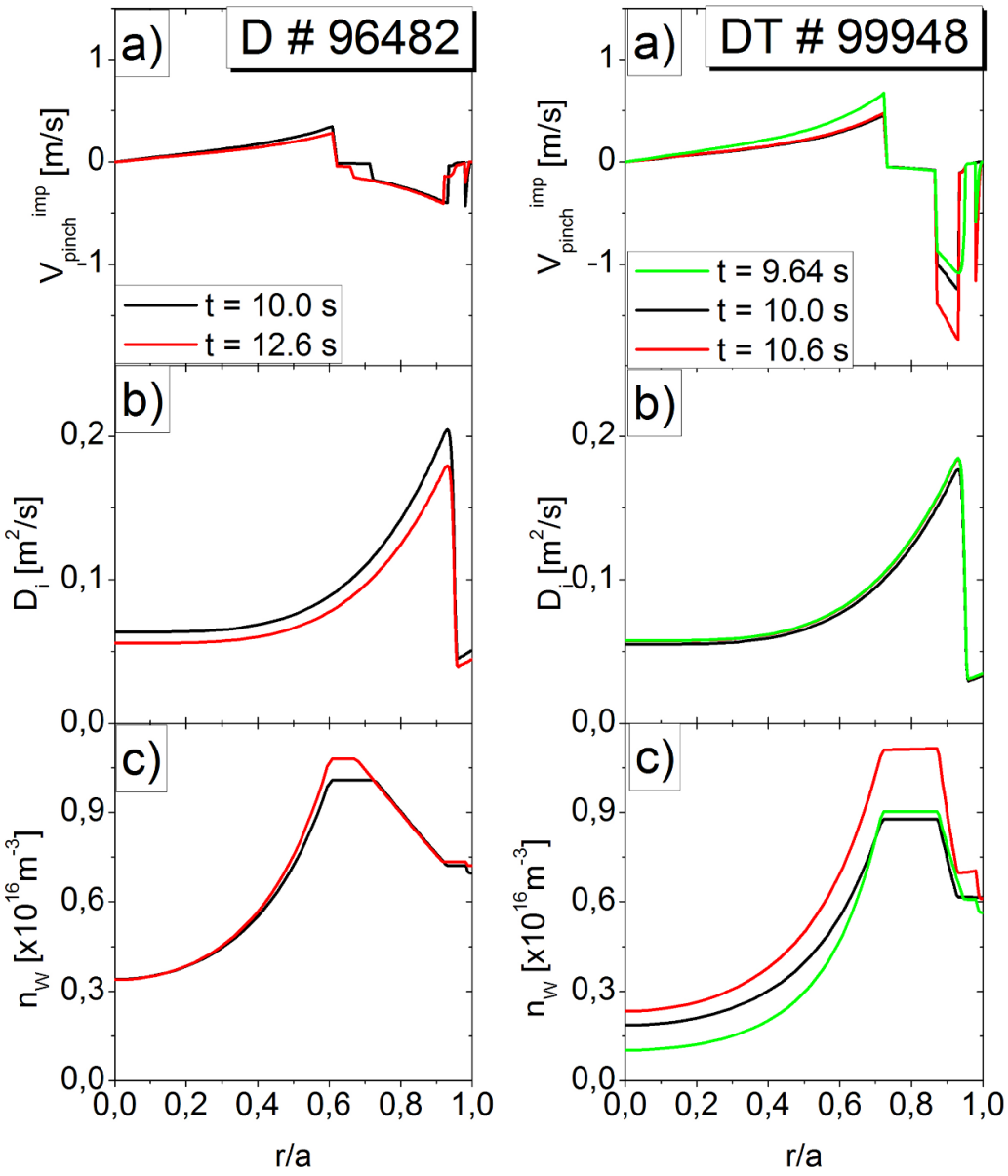

Figure 8. For the D pulse (left) and the D–T pulse (right): (*a*) convective and (*b*) diffusive impurity transport coefficients used to derive the radiation densities in figure 6, (*c*) the corresponding W densities in the hypothesis of diffusive + convective impurity transport.

to account for the total radiation level of the D–T pulse, see section 3, suggest that the 50% higher yield of the D–T pulse is compensated by the lower level of Be. The reason why the Be level is lower in the D–T pulse is not fully understood, yet. Among the possible reasons, can be considered the lower T_e at the plasma edge and the different action of the radiofrequency (RF) antennas in the two pulses. In fact, the RF sheaths are a local effect from the individual antennas. If different antennas are powered, or at different individual power levels, this can affect the Be source differently. To this point, remember, please, that in D–T pulses one RF antenna was not operational.

The increased divertor impurity screening capability of the D–T pulse and the lower W flux in the D–T pulse are not sufficient to compensate for the increase in time of the radiation, which is proportional to the increase of $<n_e>$, from about 9.6 s until the loss power approaches the H–L threshold power at ≈10.3 s and the ELMs are gradually lost. We have seen in section 3 that at this same time the amplitude of the $n = 3$ TM increases significantly as the possible effect of the current profile modification caused by enhanced LFS radiation. With respect to this point, it should be noted that not only the level of the total radiated power, but also its distribution matters. For example, at 10.0 s of the D–T pulse the hollow density profile leads to a radiation density at the plasma edge significantly higher than that of the D pulse at 12.6 s (with peaked density profile), although the total central-plasma radiated power in the D–T pulse is comparable to that of the D pulse or even lower. This strong difference in the electron density profile shape between D and D–T Baseline pulses, which is even more marked for tritium pulses, underlies many of the changes in performance and behaviour of the pulses with isotope mass.

The COREDIV results show only minor differences in W transport in the D–T pulse between 9.64 s and 10.0 s. Within the uncertainties of the measurements, this is confirmed by the experimental ratio of the total radiated power to the volume averaged electron density, which is practically the same at the two times: $P^{\mathrm{rad}}{}_{\mathrm{tot}}/< n_{\mathrm{e}} > \approx 2.0$ MW m^3 10^{-19}.

Even though qualitative differences are not seen in the COREDIV reconstruction of the W sources and transport in D and D–T Baseline JET-ILW pulses, it remains the experimental difficulty of keeping the plasma relatively stationary for 4–5 s in the D–T pulse. In principle, two ways can be pursued to alleviate this difficulty: the increase of the auxiliary power level and the control of the electron density and of the radiated power, for example, by increasing the gas puff fuelling rate. Both can keep the plasma sufficiently far from the H–L threshold thus avoiding the runaway of the core radiated power. In fact, the increase of the gas fuelling rate generally leads to the increase of the turbulent transport, causing the decrease of both energy and particle confinement and the increase in ELM frequency, with related enhancement of the impurity flushing and reduction of the radiated power level. It might be mentioned here that in recent experiments of Ne seeding in JET-ILW [30] the gas puff level in T plasmas had to be increased by a factor of 7 with respect to the corresponding D plasmas to reach the same ELM frequency in T as in D pulses, while the electron density level was nearly unchanged.

In summary, the experimental electron density and temperature profiles as well as the ion temperature profiles of the two best performing high current–high power Baseline D and D–T pulses in JET-ILW have been successfully simulated with the COREDIV model. In the absence of essential data, such as the W concentration in the plasma core and the electron temperature and density at the divertor plate, the numerical results have been compared with the experimentally reconstructed radiation profiles in the main plasma and with the total radiated power in the divertor.

The numerical impurity transport coefficients, as derived by imposing convective velocities '*ad hoc*' to fit the experimental radiated power profiles of the pulses, are only partly in agreement with the predictions of collisional and NC impurity transport theory, in which the flushing action of the ELMs is not taken into account. The COREDIV computed total W ion content, in the range of 6–8 $\times$ 10^{17} ions, is lower by about 20% for the D–T pulse and the computed W concentration, in the range of 1 $\times$ 10^{-4}, is lower by about 40% for the D–T pulse as compared with the D pulse (see table 1), due to the lower W flux and to the higher electron density. Since the COREDIV computed ratio of the W fluxes to the W densities is similar for the two pulses, it follows that the W residence time (τ_{W} of the order of 0.17 s) is similar for the D and D–T pulses. Only at the beginning of the radiation runaway, at $\approx$ 10.6 s, τ_{W} of the D–T pulse increases, simultaneously with the strong increase of the $= 3$ TM amplitude. The COREDIV computed parallel forces in the divertor show that the ratio of the collisional drag to the thermal force is higher in the D–T pulse, resulting in a better impurity divertor retention capability by about 10%. Given that significant differences in W transport and sources are not computed for the simulations of the two pulses (up to $\approx$10.0 s for the D–T pulse), it appears that the increase in time of the radiated power until the H–L threshold power is approached and the flushing action of the ELMs starts to be lost is caused by the uncontrolled increase in time of the electron density in the D–T pulse. In conclusion, control of the electron density and/or of the ELM flushing activity appears to be mandatory to reach stable conditions for these high current–high power D–T pulses in JET-ILW.

Acknowledgments

One of the authors (G. T.) wishes to thank the Referees for their comments and suggestions, which have improved the quality of this paper.

This scientific paper has been published as part of the international project co-financed by the Polish Ministry of Science and Higher Education within the programme called 'PMW' for 2024.

This work has been carried out within the framework of the EUROfusion Consortium, funded by the European Union via the Euratom Research and Training Programme (Grant Agreement No. 101052200—EUROfusion). Views and opinions expressed are however those of the author(s) only and do not necessarily reflect those of the European Union or the European Commission. Neither the European Union nor the European Commission can be held responsible for them.

ORCID iDs

A.R. Field https://orcid.org/0000-0003-0671-9668
I. Ivanova-Stanik https://orcid.org/0000-0002-2766-8612
S. Brezinsek https://orcid.org/0000-0002-7213-3326
A. Chomiczewska https://orcid.org/0000-0003-4931-728X
L. Garzotti https://orcid.org/0000-0002-3796-9814
G. Pucella https://orcid.org/0000-0002-9923-2770
D. Van Eester https://orcid.org/0000-0002-4284-3992

References

[1] Matthews G.F. *et al* 2013 *J. Nucl. Mater.* **438** S2–S10
[2] Hobirk J. *et al* 2023 *Nucl. Fusion* **63** 112001
[3] Garzotti L. *et al* Development of high current baseline scenario for high deuterium-tritium fusion performance at JET *29th Fusion Energy Conf.* (*London, UK, 16–21 October 2023*) Paper EX 7–3/1943
[4] Field A.R. *et al* 2021 *Plasma Phys. Control. Fusion* **63** 095013
[5] Field A.R. *et al* 2023 *Nucl. Fusion* **63** 016028
[6] Garcia J. *et al* 2020 Integrated scenario development at JET for DT operation and ITER risk mitigation *2020 IAEA Fusion Energy Conf. 2021* (*Nice, France, 17–20 October 2020)* (available at: https://nucleus.iaea.org/sites/fusionportal/Shared%20Documents/FEC%202020/fec2020-material/slides 0989.pdf)
[7] de la Luna E. *et al* 2020 Exploring the physics of a high performance H-mode with small ELMs and zero gas dosing in JET *2020 IAEA Fusion Energy Conf. 2021* (*Nice, France, 17–20 October 2020)* (available at: https://nucleus.iaea.org/sites/fusionportal/Shared%20Documents/FEC%202020/fec2020-preprints/preprint 1094.pdf)

[8] Czarnecka A. *et al* 2019 *Plasma Phys. Control. Fusion* **61** 085004
[9] Den Harder N., Brezinsek S., Pütterich T., Fedorczak N., Matthews G.F., Meigs A., Stamp M.F., van de Sanden M.C.M. and Van Rooij G.J. 2016 *Nucl. Fusion* **56** 026014
[10] Zagorski R., Ivanova-Stanik R.I. and Stankiewicz R. 2013 *Nucl. Fusion* **53** 073030
[11] Telesca G. *et al* 2021 *Nucl. Fusion* **61** 066027
[12] Mandrekas J. and Stacey W.M. 1995 *Nucl. Fusion* **35** 843
[13] Valisa M. *et al* 2017 The role of ELMs' and inter-ELM phases in the transport of impurities in JET *44th EPS Conf. on Plasma Physics* (*Belfast, UK, 26–30 June 2017*) p P4. 174 (available at: http://ocs.ciemat.es/EPS2017PAP/pdf/P4.174.pdf)
[14] Braginskii S.I. 1965 *Rev. Plasma Phys.* **1** 205
[15] Zagorski R. *et al* 1996 *J. Technol. Phys.* **37** 7
[16] Ivanova-Stanik I. and Zagarski R. 2015 *J. Nucl. Mater.* **463** 596–600
[17] Garcia-Rosales C., Eckstein W. and Roth J. 1994 *J. Nucl. Mater.* **218** 8–17
[18] Puetterich T. *et al* 2008 *Plasma Phys. Control. Fusion* **50** 085016
[19] Telesca G., Zagorski R., Brezinsek S., Fundamenski W., Giroud C., Maddison G., Mullane M.O., Rapp J., Stamp M. and Van Oost G. 2011 *Plasma Phys. Control. Fusion* **53** 115002
[20] Ho A. *et al* 2023 *Nucl. Fusion* **63** 066014
[21] Frassinetti L. *et al* 2023 *Nucl. Fusion* **63** 112009
[22] (Available at: https://open.adas.ac.uk/)
[23] Pucella G. *et al* 2021 *Nucl. Fusion* **61** 046020
[24] Fedorczak N. *et al* 2015 *J. Nucl. Mater.* **463** 85–90
[25] Claassen H.A. and Repp H. 1981 *Nucl. Fusion* **21** 589
[26] Neuhauser J., Schneider W., Wunderlich R. and Lackner K. 1984 *Nucl. Fusion* **24** 39
[27] Fussmann G., Field A.R., Kallenbach A., Krieger K. and Steuer K.H. (The ASDEX Team) 1991 *Plasma Phys. Control. Fusion* **33** 1677
[28] Angioni C. and Helander P. 2014 *Plasma Phys. Control. Fusion* **56** 124001
[29] Brezinsek S. *et al* 2019 *Nucl. Fusion* **59** 096035
[30] Giroud C. *et al* 2023 Core-edge integrated neon-seeded scenario in deuterium-tritium at JET *2023 Fusion Energy Conf.* (*London*, *16–21 October 2023*) Paper EX-P5/2322